Supplementary Information to 'Phonon screening and dissociation of excitons at finite temperatures from first principles'

Antonios M. Alvertis[1,2], Jonah B. Haber[3,2], Zhenglu Li[4,2,5], Christopher J. N. Coveney[6], Steven G. Louie[2,5], Marina R. Filip[6], Jeffrey B. Neaton[2,5,7,*]

[1]KBR, Inc., NASA Ames Research Center, Moffett Field, California 94035, United States
[2]Materials Sciences Division, Lawrence Berkeley National Laboratory, Berkeley, California 94720, United States
[3]Department of Materials Science and Engineering, Stanford University, Stanford, California 94305, United States
[4]Mork Family Department of Chemical Engineering and Materials Science, University of Southern California, Los Angeles, California 90089, United States
[5]Department of Physics, University of California Berkeley, Berkeley, United States
[6]Department of Physics, University of Oxford, Oxford OX1 3PJ, United Kingdom
[7]Kavli Energy NanoScience Institute at Berkeley, Berkeley, United States
[*]e-mail: jbneaton@lbl.gov

Contents

Material	Structure	a (Å)	c/a	Space Group	Identifier
AlN	Wurtzite	3.128	1.604	$P6_3mc$	mp-661
CdS	Zincblende	4.200	1	$F\bar{4}3m$	mp-2469
GaN	Wurtzite	3.215	1.630	$P6_3mc$	mp-804
MgO	Halite, Rock Salt	3.010	1	$Fm\bar{3}m$	mp-1265
$SrTiO_3$	Cubic Perovskite	3.852	1	$Pm\bar{3}m$	mp-5229

Table S1 Studied materials, their structure, lattice parameters, space group, and identifier in the Materials Project database [1]. We performed geometry optimization for the atomic positions of these systems using DFT within the PBE exchange-correlation functional, keeping their lattice parameters fixed, with the exception of $SrTiO_3$, for which we used the local density approximation (LDA) and optimized both the atomic positions and its lattice parameter (the LDA has been discussed in the literature to yield more accurate results for structural properties of $SrTiO_3$ compared to PBE [2]).

S1 Computational Details

Table S1 summarizes the different systems studied in this work, the specific structure in which these are studied, their lattice parameter, as well as their space group and identifier in the Materials Project database [1]. For all studied materials with the exception of $SrTiO_3$, we start by performing a geometry optimization of their atomic positions, leaving the lattice parameters fixed. For this we employ DFT, as implemented within the Quantum Espresso software package [3], and we use the generalized gradient approximation (GGA) as formulated by Perdew, Burke and Ernzerhof (PBE) [4]. For $SrTiO_3$ we employ the local density approximation (LDA) [5] and optimize both the atomic positions and lattice parameters of this system; the LDA has been discussed in the literature to yield more accurate results for the phonon properties of $SrTiO_3$ compared to PBE [2]. For all calculations we employ scalar-relativistic optimized norm-conserving Vanderbilt pseudopotentials (ONCV) [6] with standard accuracy, taken from Pseudo Dojo [7]. Specifically, these include three valence electrons for Ga, two valence electrons for Al, three valence electrons for Sr, four valence electrons for Ti, two valence electrons for O, two valence electrons for N, two valence electrons for S, three valence electrons for Mg, and four valence electrons for Cd. We employ DFPT using PBE, with the exception of $SrTiO_3$ for which we employ LDA to compute the phonon dispersions of the studied materials on a $6 \times 6 \times 6$ grid of $\mathbf{q}$-points. Using the DFT-PBE Kohn-Sham wavefunctions (LDA for $SrTiO_3$) as a starting point, we perform *GW* calculations as implemented within the BerkeleyGW code [8], choosing the calculation parameters to converge the quasiparticle band gaps within 0.1 eV, following Refs. [9, 10] and using a generalized plasmon pole model [11] to compute the dielectric function at finite frequencies. Specifically, we employ the following parameters for the *GW* calculation: AlN (400 bands, 32 Ry polarizability cutoff, $6 \times 6 \times 6$ half-shifted k-grid), CdS (500 bands, 40 Ry polarizability cutoff, $6 \times 6 \times 6$ half-shifted k-grid), GaN (400 bands, 40 Ry polarizability cutoff, $4 \times 4 \times 4$ half-shifted k-grid), MgO (600 bands, 50 Ry polarizability cutoff, $6 \times 6 \times 6$ Γ-centered k-grid), $SrTiO_3$ (1000 bands, 14 Ry polarizability cutoff, $6 \times 6 \times 6$ half-shifted k-grid). Moreover, we have verified the validity of the plasmon pole approximation, by comparing the computed exciton binding energies for the example cases of CdS and MgO to those obtained when computing the dielectric function within full frequency calculations. We find that this leads to a change of less than 0.5 meV to the computed values.

The electronic BSE kernel is computed on the same $\mathbf{k}$-grid as the *GW* eigenvalues, for four valence and four conduction bands, with the exception of $SrTiO_3$, where nine valence bands and three conduction bands

are employed instead. For $SrTiO_3$, the valence and conduction bands that the kernel is computed on are disentangled from other bands, we can therefore interpolate the kernel on a dense grid, for the same bands. For the remaining systems we interpolate the kernel on a fine grid, for three valence and a single conduction band. For all cases, we use the patched sampling technique [12] to interpolate the kernel onto a patch drawn from a fine $100 \times 100 \times 100$ grid, converging the size of the patch to ensure an accuracy of 1 meV or better for the exciton binding energy, as described in detail in Ref. [12]. We find that a patch around Γ with a crystal coordinate cutoff of 0.09 is sufficient to converge the observables of interest in this study for all systems but MgO and $SrTiO_3$. For these two systems we extrapolate to the $N_k \to \infty$ limit by following the convergence rate of the value of $\Delta E_B^{\text{F-H}}$ obtained through the numerical integration of Eq. (19) of the main manuscript (see Section S5). Furthermore, we have tested the impact of computing the kernel on a coarse grid with more valence and conduction bands prior to interpolation, for all systems but $SrTiO_3$. Computing the kernel on 8 valence and 8 conduction bands results in a change of less than 1 meV for the computed exciton binding energies.

To obtain the electron-phonon matrix elements $g_{mn\nu}(\mathbf{k}, \mathbf{q})$ on the same fine patch for the **k**- and **q**-grid we employ Wannier-Fourier interpolation [13], using modified versions of the Wannier90 [14] and EPW [15] codes, in order to ensure the gauge consistency of the electron-phonon matrix elements computed from EPW and the exciton coefficients computed using BerkeleyGW, using a workflow that will be described elsewhere [16].

Material	m_e (a.u.)	m_h (a.u.)	a_o (Å)	r_e (Å)	r_h (Å)
AlN	0.30	0.70	11.3	10.8	7.0
CdS	0.12	2.01	29.4	30.5	7.5
GaN	0.15	1.01	21.1	17.3	6.7
MgO	0.34	5.00	6.1	11.6	3.0
$SrTiO_3$	0.39	1.22	10.2	9.9	5.6

Table S2 Estimated exciton Bohr radii a_o, electron-/hole-polaron radii $r_{e,h}$, and electron/hole effective masses $m_{e,h}$ of the studied systems.

S2 Estimated exciton and polaron radii of studied systems

Table S2 summarizes the exciton Bohr radius a_o and the electron-/hole-polaron radii $r_{e,h}$ of the studied systems. The exciton bohr radius is estimated as $a_o = 1/(2E_B\mu)^{1/2}$ within the Wannier-Mott model, where E_B the converged BSE exciton binding energies given in Table I of the main manuscript, and μ the exciton effective mass $1/\mu = 1/m_e + 1/m_h$, with m_e and m_h the effective mass of the electron and hole, respectively. A more quantitatively accurate calculation of the exciton radius would require using first-principles methods that accurately capture this quantity [17]. The estimated electron-/hole-polaron radii are obtained as $r_{e,h} = \frac{1}{\sqrt{2m_{e,h}\omega_{LO}}}$ [18], under the assumption of weak, Fröhlich-like electron-phonon coupling. While recent development of first-principles methodologies now allows more accurate computation of the spatial extent of electron and hole polarons [19], the values reported in Table S2 indicate that our studied materials are within the regime where the lattice polarization associated with the two polarons may interfere significantly, as described elsewhere [20, 21].

Moreover, Table S2 summarizes the electron and hole effective masses. We compute the effective masses for the top/bottom of the valence and conduction bands respectively using the finite difference formula $\frac{1}{m^*} = \frac{E(\delta\mathbf{k})+E(-\delta\mathbf{k})-2E(\Gamma)}{\delta\mathbf{k}^2}$, taking $\delta\mathbf{k}$ to be equal to 0.01 (in crystal coordinates) along each spatial direction, and we average over the three spatial directions. The energies E are computed at the GW level.

S3 Finite temperature expression for phonon kernel

At zero temperature the phonon kernel is written as

$$K^{ph}_{cv\mathbf{k},c'v'\mathbf{k}'}(\Omega) = \langle cv\mathbf{k}| \frac{1}{2\pi i}\int_{-\infty}^{\infty} d\omega\, W^{ph}(\mathbf{r},\mathbf{r}';\omega)\left[\frac{1}{\Omega-\omega-(\epsilon_{c'\mathbf{k}'}-\epsilon_{v\mathbf{k}})+i\eta}+\frac{1}{\Omega+\omega-(\epsilon_{c\mathbf{k}}-\epsilon_{v'\mathbf{k}'})+i\eta}\right] e^{-i\eta\omega}\,|c'v'\mathbf{k}'\rangle \tag{1}$$

The kernel can be analytically continued into the complex plane $\omega \to z$ and then evaluated at the boson imaginary Matsubara frequencies as the screened interaction is proportional to the bosonic phonon propagator. To proceed, we write the expression for phonon screening in a simpler form

$$W^{ph}(\mathbf{r},\mathbf{r}';z) = \sum_{\mathbf{q}\nu} g^*_\nu(\mathbf{r}')D_{\mathbf{q}\nu}(z)g_\nu(\mathbf{r}) = \sum_\nu g^*_\nu(\mathbf{r}')\frac{2\omega_{\mathbf{q}\nu}}{z^2-\omega^2_{\mathbf{q}.\nu}}g_\nu(\mathbf{r}). \tag{2}$$

Evaluating the frequency convolution at finite temperature requires the summation over the discrete bosonic Matsubara frequencies $i\Omega_m/i\omega_n$, so we can write $K(\Omega)\to K(i\Omega_m)$ and $i\Omega_n/i\omega_n = i\frac{2\pi n}{\beta}$ which gives

$$K^{ph}_{cv\mathbf{k},c'v'\mathbf{k}'}(i\Omega_m) = \frac{1}{\beta}\sum_{\mathbf{q}\nu}\sum_{i\omega_n} g_{cc'\nu}(\mathbf{k}',\mathbf{q})g^*_{vv'\nu}(\mathbf{k}',\mathbf{q})D_{\mathbf{q}\nu}(i\omega_n)\left[\frac{1}{i\Omega_m+i\omega_n-(\epsilon_{c'\mathbf{k}'}-\epsilon_{v\mathbf{k}})}+\frac{1}{i\Omega_m+i\omega_n-(\epsilon_{c\mathbf{k}}-\epsilon_{v'\mathbf{k}'})}\right]. \tag{3}$$

The way to evaluate these summations is by first evaluating the contour integral of infinite radius, which contains all the poles of the function. This integral is weighted by the boson occupation factor $n_B(z)$ which contains simple poles at all the Matsubara frequencies, all of equal residue $\frac{1}{\beta}$. Then we send the contour to zero radius as the result is independent of the radius of the path to obtain the result of the summation

$$I = \oint_C \frac{dz}{2\pi i} f(z)n_B(z) = \sum_i Res(a_i), \tag{4}$$

where

$$f(z) = D_{\mathbf{q}\nu}(z)\left[\frac{1}{i\Omega_m+z-(\epsilon_{c'\mathbf{k}'}-\epsilon_{v\mathbf{k}})}+\frac{1}{i\Omega_m+z-(\epsilon_{c\mathbf{k}}-\epsilon_{v'\mathbf{k}'})}\right]. \tag{5}$$

The poles of $f(z)$ occur at

$$\begin{aligned} a_1 &= +\omega_{\mathbf{q}\nu} \\ a_2 &= -\omega_{\mathbf{q}\nu} \\ a_3 &= (\epsilon_{c'\mathbf{k}'}-\epsilon_{v\mathbf{k}}) - i\Omega_m \\ a_4 &= (\epsilon_{c\mathbf{k}}-\epsilon_{v'\mathbf{k}'}) - i\Omega_m \\ a_n &= i\omega_n = i\frac{2\pi n}{\beta}. \end{aligned} \tag{6}$$

Evaluation of this integral therefore gives (dropping the summation over the phonon modes)

$$\begin{aligned} I = \frac{1}{\beta}\sum_{i\omega_n} D_{\mathbf{q}\nu}(i\omega_n)\left[\frac{1}{i\Omega_m + i\omega_n - (\epsilon_{c'\mathbf{k}'} - \epsilon_{v\mathbf{k}})} + \frac{1}{i\Omega_m + i\omega_n - (\epsilon_{c\mathbf{k}} - \epsilon_{v'\mathbf{k}'})}\right] + \\ N_B(\omega_{\mathbf{q}\nu})\left[\frac{1}{i\Omega_m + \omega_{\mathbf{q}\nu} - (\epsilon_{c'\mathbf{k}'} - \epsilon_{v\mathbf{k}})} + \frac{1}{i\Omega_m + \omega_{\mathbf{q}\nu} - (\epsilon_{c\mathbf{k}} - \epsilon_{v'\mathbf{k}'})}\right] + \\ N_B(-\omega_{\mathbf{q}\nu})\left[\frac{1}{i\Omega_m - \omega_{\mathbf{q}\nu} - (\epsilon_{c'\mathbf{k}'} - \epsilon_{v\mathbf{k}})} + \frac{1}{i\Omega_m - \omega_{\mathbf{q}\nu} - (\epsilon_{c\mathbf{k}} - \epsilon_{v'\mathbf{k}'})}\right] + \\ 2\omega_{\mathbf{q}\nu}\left[\frac{N_B((\epsilon_{c'\mathbf{k}'} - \epsilon_{v\mathbf{k}}) - i\Omega_m)}{((\epsilon_{c'\mathbf{k}'} - \epsilon_{v\mathbf{k}}) - i\Omega_m)^2 - \omega_{\mathbf{q}\nu}^2} + \frac{N_B((\epsilon_{c\mathbf{k}} - \epsilon_{v'\mathbf{k}'}) - i\Omega_m)}{((\epsilon_{c\mathbf{k}} - \epsilon_{v'\mathbf{k}'}) - i\Omega_m)^2 - \omega_{\mathbf{q}\nu}^2}\right]. \end{aligned} \tag{7}$$

We now send the contour radius to zero, since the result is independent of this quantity. This means we can evaluate the Matsubara frequency summation which gives the kernel

$$\begin{aligned} -K^{ph}_{cv\mathbf{k},c'v'\mathbf{k}'}(i\Omega_m) = N_B(\omega_{\mathbf{q}\nu})\left[\frac{1}{i\Omega_m + \omega_{\mathbf{q}\nu} - (\epsilon_{c'\mathbf{k}'} - \epsilon_{v\mathbf{k}})} + \frac{1}{i\Omega_m + \omega_{\mathbf{q}\nu} - (\epsilon_{c\mathbf{k}} - \epsilon_{v'\mathbf{k}'})}\right] + \\ N_B(-\omega_{\mathbf{q}\nu})\left[\frac{1}{i\Omega_m - \omega_{\mathbf{q}\nu} - (\epsilon_{c'\mathbf{k}'} - \epsilon_{v\mathbf{k}})} + \frac{1}{i\Omega_m - \omega_{\mathbf{q}\nu} - (\epsilon_{c\mathbf{k}} - \epsilon_{v'\mathbf{k}'})}\right] + \\ 2\omega_{\mathbf{q}\nu}\left[\frac{N_B((\epsilon_{c'\mathbf{k}'} - \epsilon_{v\mathbf{k}}) - i\Omega_m)}{((\epsilon_{c'} - \epsilon_{v\mathbf{k}}) - i\Omega_m)^2 - \omega_{\mathbf{q}\nu}^2} + \frac{N_B((\epsilon_{c\mathbf{k}} - \epsilon_{v'\mathbf{k}'}) - i\Omega_m)}{((\epsilon_{c\mathbf{k}} - \epsilon_{v'\mathbf{k}'}) - i\Omega_m)^2 - \omega_{\mathbf{q}\nu}^2}\right] \end{aligned} \tag{8}$$

Now, noting that $N_B((\epsilon_{c'} - \epsilon_v) - i\Omega_m) = N_B(\epsilon_{c'} - \epsilon_v)$ (for $i\Omega_m$ as bosonic Matsubara frequencies) and that $N_B(-\omega_{\mathbf{q}\nu}) = N_B(\omega_{\mathbf{q}\nu}) + 1$, we can rewrite this as

$$\begin{aligned} -K^{ph}_{cv\mathbf{k},c'v'\mathbf{k}'}(i\Omega_m) = N_B(\omega_{\mathbf{q}\nu})\left[\frac{1}{i\Omega_m + \omega_{\mathbf{q}\nu} - (\epsilon_{c'\mathbf{k}'} - \epsilon_{v\mathbf{k}})} + \frac{1}{i\Omega_m + \omega_{\mathbf{q}\nu} - (\epsilon_{c\mathbf{k}} - \epsilon_{v'\mathbf{k}'})}\right] + \\ [N_B(\omega_{\mathbf{q}\nu}) + 1]\left[\frac{1}{i\Omega_m - \omega_{\mathbf{q}\nu} - (\epsilon_{c'\mathbf{k}'} - \epsilon_{v\mathbf{k}})} + \frac{1}{i\Omega_m - \omega_{\mathbf{q}\nu} - (\epsilon_{c\mathbf{k}} - \epsilon_{v'\mathbf{k}'})}\right] - \\ 2\omega_{\mathbf{q}\nu}\left[\frac{N_B(\epsilon_{c'\mathbf{k}'} - \epsilon_{v\mathbf{k}})}{((\epsilon_{c'\mathbf{k}'} - \epsilon_{v\mathbf{k}}) - i\Omega_m)^2 - \omega_{\mathbf{q}\nu}^2} + \frac{N_B(\epsilon_{c\mathbf{k}} - \epsilon_{v'\mathbf{k}'})}{((\epsilon_{c\mathbf{k}} - \epsilon_{v'\mathbf{k}'}) - i\Omega_m)^2 - \omega_{\mathbf{q}\nu}^2}\right] \end{aligned} \tag{9}$$

Finally, we can split the last two terms into their partial fractions as

$$\frac{2\omega_{\mathbf{q}\nu}}{((\epsilon_{c'\mathbf{k}'} - \epsilon_{v\mathbf{k}}) - i\Omega_m)^2 - \omega_{\mathbf{q}\nu}^2} = \frac{1}{i\Omega_m - (\epsilon_{c'\mathbf{k}'} - \epsilon_{v\mathbf{k}}) - \omega_{\mathbf{q}\nu}} - \frac{1}{i\Omega_m - (\epsilon_{c'\mathbf{k}'} - \epsilon_{v\mathbf{k}}) + \omega_{\mathbf{q}\nu}} \tag{10}$$

which gives

$$\begin{aligned} -K^{ph}_{cv\mathbf{k},c'v'\mathbf{k}'}(i\Omega_m) = &N_B(\omega_{\mathbf{q}\nu})\left[\frac{1}{i\Omega_m + \omega_{\mathbf{q}\nu} - (\epsilon_{c'\mathbf{k}'} - \epsilon_{v\mathbf{k}})} + \frac{1}{i\Omega_m + \omega_{\mathbf{q}\nu} - (\epsilon_{c\mathbf{k}} - \epsilon_{v'\mathbf{k}'})}\right] + \\ &[N_B(\omega_{\mathbf{q}\nu}) + 1]\left[\frac{1}{i\Omega_m - \omega_{\mathbf{q}\nu} - (\epsilon_{c'\mathbf{k}'} - \epsilon_{v\mathbf{k}})} + \frac{1}{i\Omega_m - \omega_{\mathbf{q}\nu} - (\epsilon_{c\mathbf{k}} - \epsilon_{v'\mathbf{k}'})}\right] + \\ &N_B(\epsilon_{c'\mathbf{k}'} - \epsilon_{v\mathbf{k}})\left[\frac{1}{i\Omega_m - (\epsilon_{c'\mathbf{k}'} - \epsilon_{v\mathbf{k}}) - \omega_{\mathbf{q}\nu}} - \frac{1}{i\Omega_m - (\epsilon_{c'\mathbf{k}'} - \epsilon_{v\mathbf{k}}) + \omega_{\mathbf{q}\nu}}\right] + \\ &N_B(\epsilon_{c\mathbf{k}} - \epsilon_{v'\mathbf{k}'})\left[\frac{1}{i\Omega_m - (\epsilon_{c\mathbf{k}} - \epsilon_{v'\mathbf{k}'}) - \omega_{\mathbf{q}\nu}} - \frac{1}{i\Omega_m - (\epsilon_{c\mathbf{k}} - \epsilon_{v'\mathbf{k}'}) + \omega_{\mathbf{q}\nu}}\right]. \end{aligned} \tag{11}$$

This expression simplifies to

$$-K^{ph}_{cv\mathbf{k},c'v'\mathbf{k}'}(i\Omega_m) = \frac{N_B(\omega_{\mathbf{q}\nu}) - N_B(\epsilon_{c'\mathbf{k}'} - \epsilon_{v\mathbf{k}})}{i\Omega_m + \omega_{\mathbf{q}\nu} - (\epsilon_{c'\mathbf{k}'} - \epsilon_{v\mathbf{k}})} + \frac{N_B(\omega_{\mathbf{q}\nu}) - N_B(\epsilon_{c\mathbf{k}} - \epsilon_{v'\mathbf{k}'})}{i\Omega_m + \omega_{\mathbf{q}\nu} - (\epsilon_{c\mathbf{k}} - \epsilon_{v'\mathbf{k}'})} + \frac{N_B(\omega_{\mathbf{q}\nu}) + 1 + N_B(\epsilon_{c'\mathbf{k}'} - \epsilon_{v\mathbf{k}})}{i\Omega_m - \omega_{\mathbf{q}\nu} - (\epsilon_{c'\mathbf{k}'} - \epsilon_{v\mathbf{k}})} + \frac{N_B(\omega_{\mathbf{q}\nu}) + 1 + N_B(\epsilon_{c\mathbf{k}} - \epsilon_{v'\mathbf{k}'})}{i\Omega_m - \omega_{\mathbf{q}\nu} - (\epsilon_{c\mathbf{k}} - \epsilon_{v'\mathbf{k}'})}. \tag{12}$$

The phonon kernel has four poles corresponding to the electron-hole pair absorption and emission of a phonon, which are weighted by the relevant Bose factors. Analytically continuing $i\Omega_m \to \omega + i\eta$ gives the finite temperature expression for the retarded K^{ph} and the zero temperature result is regained by sending the Bose occupation factors to zero. We now re-insert the summation over the electron-phonon vertices and phonon modes to get the full result

$$K^{ph}_{cv\mathbf{k},c'v'\mathbf{k}'}(i\Omega_m) = -\sum_{\nu} g_{cc'\nu}(\mathbf{k}', \mathbf{q}) g^{*}_{vv'\nu}(\mathbf{k}', \mathbf{q}) \left[\frac{N_B(\omega_{\mathbf{q}\nu}) - N_B(\epsilon_{c'\mathbf{k}'} - \epsilon_{v\mathbf{k}})}{i\Omega_m + \omega_{\mathbf{q}\nu} - (\epsilon_{c'\mathbf{k}'} - \epsilon_{v\mathbf{k}})} + \frac{N_B(\omega_{\mathbf{q}\nu}) - N_B(\epsilon_{c\mathbf{k}} - \epsilon_{v'\mathbf{k}'})}{i\Omega_m + \omega_{\mathbf{q}\nu} - (\epsilon_{c\mathbf{k}} - \epsilon_{v'\mathbf{k}'})} + \frac{N_B(\omega_{\mathbf{q}\nu}) + 1 + N_B(\epsilon_{c'\mathbf{k}'} - \epsilon_{v\mathbf{k}})}{i\Omega_m - \omega_{\mathbf{q}\nu} - (\epsilon_{c'\mathbf{k}'} - \epsilon_{v\mathbf{k}})} + \frac{N_B(\omega_{\mathbf{q}\nu}) + 1 + N_B(\epsilon_{c\mathbf{k}} - \epsilon_{v'\mathbf{k}'})}{i\Omega_m - \omega_{\mathbf{q}\nu} - (\epsilon_{c\mathbf{k}} - \epsilon_{v'\mathbf{k}'})} \right], \tag{13}$$

which corresponds to eq.(8) of the main manuscript.

S4 Imaginary part of the phonon kernel as an exciton dissociation rate

Here we outline in greater detail the arguments, using scattering theory and many-body perturbation theory techniques [22, 23], that establish the imaginary part of the diagonal elements of the phonon kernel in the unperturbed exciton basis as related to the rate of the dissociation channel for excitons into free electron-hole pairs, due to the absorption of a single phonon.

Within the GW-BSE formalism and accounting for phonon screening, the dynamics of a system of excitons and phonons is described by the Hamiltonian

$$H = (E_{c\mathbf{k}} - E_{v\mathbf{k}})\delta_{vv'}\delta_{cc'}\delta_{\mathbf{k}\mathbf{k}'} + K^{eh}_{cv\mathbf{k},c'v'\mathbf{k}'} + H_{ph} + K^{ph}_{cv\mathbf{k},c'v'\mathbf{k}'}, \tag{14}$$

where H_{ph} is the phonon Hamiltonian and $H_{\mathrm{BSE}} = (E_{c\mathbf{k}} - E_{v\mathbf{k}})\delta_{vv'}\delta_{cc'}\delta_{\mathbf{k}\mathbf{k}'} + K^{eh}_{cv\mathbf{k},c'v'\mathbf{k}'}$ is the usual bare BSE Hamiltonian.

At temperature T the initial (bare exciton) state of Fig. 1 of the main manuscript is a particular eigenstate of the Hamiltonian $H_i = H_{\mathrm{BSE}} + H_{ph}$:

$$H_i \left|S, N_B + 1\right\rangle = E_i^S \left|S, N_B + 1\right\rangle, \tag{15}$$

with energy $E_i^S = \Omega_S + (N_B + 1)\omega_{LO}$. We consider here the example of an LO phonon with occupation N_B at temperature T, but the same holds for any phonon mode. The absorption of a single phonon can lead to a final (free electron-hole) state, which also can be expressed as an eigenstate of the distinct but related Hamiltonian $H_f = (E_{c\mathbf{k}} - E_{v\mathbf{k}})\delta_{vv'}\delta_{cc'}\delta_{\mathbf{k}\mathbf{k}'} + H_{ph}$, where

$$H_f \left|(c\mathbf{k}, v\mathbf{k}'), N_B\right\rangle = E_f \left|(c\mathbf{k}, v\mathbf{k}'), N_B\right\rangle, \tag{16}$$

with $E_f = E_{c\mathbf{k}} - E_{v\mathbf{k}'} + N_B\omega_{LO}$. The initial and final states are described as eigenstates of different Hamiltonians, apparently complicating a straightforward interpretation of the scattering process, as one needs to ensure orthogonality between these wavefunctions [24]. However, this complication is resolved using the arguments of the theory of rearrangement collisions [25, 26, 27]. We can define a renormalized final free electron-hole state $|\chi_f\rangle$, which satisfies orthogonality to the initial state $|S, N_B + 1\rangle$, as [28]

$$\left|\chi_f\right\rangle = \left|(c\mathbf{k}, v\mathbf{k}'), N_B\right\rangle + (E_f - H - i\eta)^{-1} K^{eh} \left|(c\mathbf{k}, v\mathbf{k}'), N_B\right\rangle. \tag{17}$$

State $|\chi_f\rangle$ may be used to define a generalized $\mathcal{S}$-matrix for the scattering process, which to first order in the electron-phonon interaction and within the Born approximation is written as

$$\mathcal{S}^{Born}_{gen} = 2\pi i\delta(E_f - E_i) \left\langle(c\mathbf{k}, v\mathbf{k}'), N_B\right| K^{ph} \left|S, N_B + 1\right\rangle. \tag{18}$$

Employing the optical theorem for this $\mathcal{S}$-matrix in standard fashion, $\mathrm{Im}[K_{SS}^{ph}(\Omega_S, T)]$ can be interpreted as the rate of this exciton dissociation process, namely

$$2|\mathrm{Im}[K_{SS}^{ph}(\Omega_S, T)]| \approx \tau_S^{-1}(T). \tag{19}$$

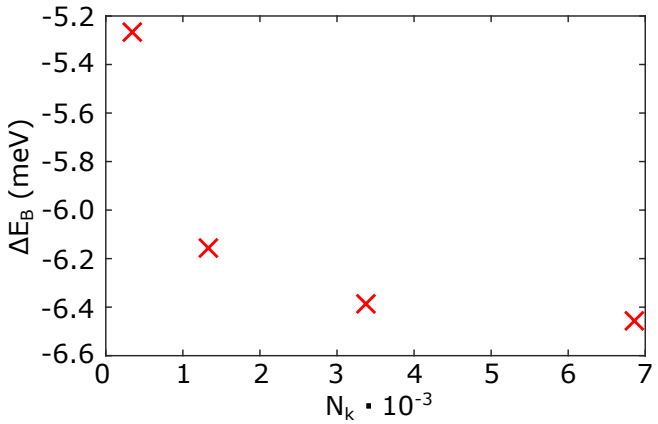

Figure S1 Convergence of the exciton binding energy shift of CdS due to phonon screening at 0 K, with respect to the number of k-points in a patch centered around the Γ-point of a $100 \times 100 \times 100$ grid.

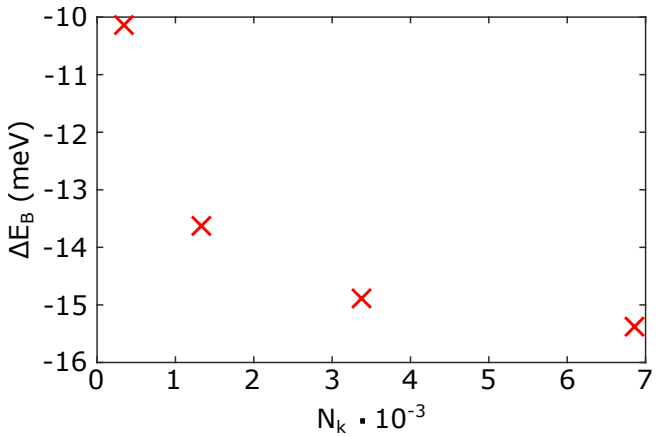

Figure S2 Convergence of the exciton binding energy shift of GaN due to phonon screening at 0 K, with respect to the number of k-points in a patch centered around the Γ-point of a $100 \times 100 \times 100$ grid.

S5 Convergence of the first-principles phonon kernel

Figures S1 and S2 demonstrate the convergence of the real part of K^{ph} in CdS and GaN respectively, *i.e.* the correction ΔE_B to their exciton binding energy from phonons. By employing a patch taken from a $100\times100\times100$ regular grid, we are able to demonstrate convergence within less than 1 meV at 0 K, for a patch cutoff of 0.09 (in crystal coordinates) around Γ, corresponding to $6,859$ $\mathbf{k}/\mathbf{q}$-points.

For $SrTiO_3$ convergence is more challenging to achieve. Fig. S3 demonstrates the values of $\Delta E^{\text{F-H}}_{B,\text{gen.}}$ contributed by the LO-1 phonon, as predicted by Eq. (19) when using the generalized Fröhlich vertex of Eq. (26). In order to fully converge ΔE_B we have to compute the sum of Eq. (19) on a grid of $29,791$ $\mathbf{k}/\mathbf{q}$-points (corresponding to a patch with a cutoff of 0.15 around Γ in crystal coordinates, drawn from a $100 \times 100 \times 100$ regular grid), which is possible to do within this numerical integration employing the hydrogenic and Fröhlich formulas. However, convergence at the same level is very challenging to achieve from first principles. When employing our *ab initio* workflow, we were able to compute the phonon kernel on a Γ-centered patch with a cutoff of 0.09 (crystal coordinates), which includes $6,859$ $\mathbf{k}/\mathbf{q}$-points, obtaining ΔE_B values of -31.1 meV and -7 meV for the LO-1 and LO-2 phonons respectively. For the same grid size, the numerical integration of Eq. (19) gives

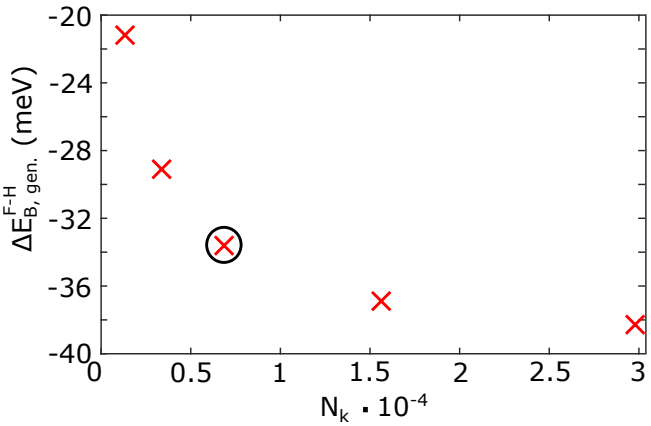

Figure S3 Convergence of the exciton binding energy shift of $SrTiO_3$ due to phonon screening from the LO-1 mode at 0 K, with respect to the number of k-points in a patch centered around the Γ-point of a $100 \times 100 \times 100$ grid, as computed through numerical integration of the approximate Eq. (19) employing the generalized Frölich vertex of Eq. (26). The point in the black circle corresponds to the maximum grid size which was accessible through our *ab initio* workflow, and which is extrapolated to the $N_k \to \infty$ limit as discussed in the text.

corrections of −33.6 meV and −7 meV for these two phonons respectively. Therefore, for the LO-2 phonon the two levels of theory are in perfect agreement at 0 K, whereas for the LO-1 phonon, the first-principles workflow gives a correction which is equal to 92.7% of the $\Delta E_{B,\text{gen.}}^{\text{F-H}}$ value of Fig. S3 on the same grid size (circled in black). Consequently, in order to estimate the *ab initio* values at the $N_k \to \infty$ limit, for the LO-1 phonon contribution to $\Delta E_B^{ab\ initio}$, we take 92.7% of the converged value of $\Delta E_{B,\text{gen.}}^{\text{F-H}}$ as estimated from Eq. (19) (−38 meV), which is equal to −35 meV (Table II main manuscript). For the LO-2 phonon the *ab initio* and the generalized Fröhlich-hydrogenic results on the patch of 6,859 $\mathbf{k}/\mathbf{q}$-points are identical, we therefore simply extrapolate the first-principles contribution to ΔE_B from this phonon from the slightly under-converged value of −7 meV, to the $N_k \to \infty$ limit of −8 meV. This same method for extrapolating to $N_k \to \infty$ is used for the phonon screening of the MgO exciton by the LO phonon of this material.

Material	Thermal Expansion Coefficient (K^{-1})	Reference	$\Delta a/a(\Delta T = 300\,K)$ (%)
AlN	$6.9 \cdot 10^{-6}$	[29]	0.2
CdS	$4.5 \cdot 10^{-6}$	[30]	0.14
GaN	$6 \cdot 10^{-6}$	[31]	0.18
MgO	$3.2 \cdot 10^{-5}$	[32]	1
$SrTiO_3$	$3 \cdot 10^{-5}$	[33]	0.9

Table S3 Thermal expansion coefficients of the studied systems, as found in the literature, and percentage of change to the a lattice constant assuming linear thermal expansion over 300 K.

S6 Effect of thermal expansion

In Table S3 we report the coefficients of linear thermal expansion of the systems we study here, as found in the literature. For $SrTiO_3$ we take a representative value for room temperature as reported for the zero external pressure case in Ref. [33]. Assuming linear thermal expansion over the temperature range $0-300\,K$, we estimate the percentage of change $\Delta a/a$ to the lattice constant over these temperatures for each material. We see in Table S3 that for AlN, CdS, and GaN, the lattice constants change by at most 0.2%, we therefore neglect this effect for the range of temperatures we are concerned with here. For MgO and $SrTiO_3$ there is a more significant change of approximately 1% to the lattice constant. For these two materials we have repeated the calculations of the bare and phonon-screened exciton binding energy, in order to evaluate the importance of thermal expansion.

Starting with MgO, expanding its lattice constant by 1% decreases the bare exciton binding energy of this system to 305 meV, compared to the 327 meV value of Table I in the main manuscript. The LO phonon frequency also decreases from 84 meV to 81 meV. However, the *ab initio* phonon screening of the exciton remains almost unchanged, with the effect reduced by a mere 0.5 meV compared to the value of Table I.

For $SrTiO_3$, upon expansion of the lattice by 1%, the bare exciton binding energy reduces from 122 meV to 107 meV, while the LO-1 phonon also reduces its energy from 98 meV to 94 meV. While we were not able to obtain fully first-principles values for the phonon screening of the exciton of $SrTiO_3$ at this modified configuration due to the emergence of imaginary phonons, taking the $\mathbf{q} \to \mathbf{0}$ limit and using the model of Eq. (25) of the main manuscript, we obtain $\Delta E_B^{\mathbf{q}\to\mathbf{0}} = -61$ meV, compared to $\Delta E_B^{\mathbf{q}\to\mathbf{0}} = -65$ meV when not accounting for thermal expansion, which suggests a 6% decrease in the effect of phonon screening on the exciton binding energy.

Overall, we find that the effect of thermal expansion can lead to a small decrease of the screening of the exciton from phonons. This change in phonon screening is generally modest due to the fact that *both* ω_{LO} and E_B are reduced upon expansion of the lattice, making the change in their ratio less significant. The reduction of the exciton binding energy due to thermal expansion, combined with the small effect of thermal expansion on phonon screening, will result to an overall larger decrease of exciton binding energies when thermal expansion and phonon screening are accounted for concurrently, and lead to better agreement with experimental values. Nevertheless, the temperature-dependent reduction of exciton binding energies due to phonon screening remains the dominant effect, as seen here even for MgO and $SrTiO_3$, the systems with the greatest effect of thermal expansion among the studied ones.

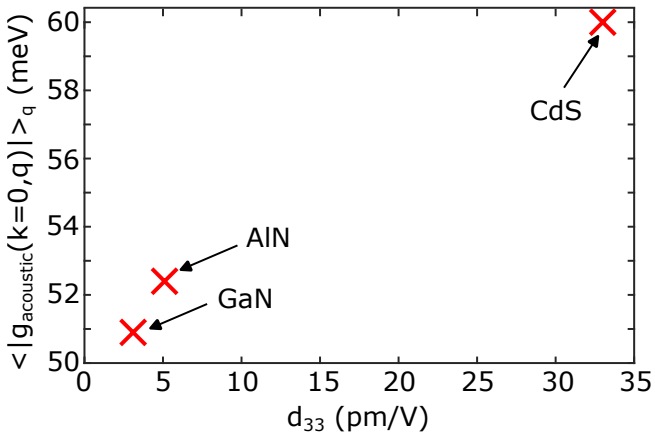

Figure S4 Average electron-phonon coupling of acoustic modes of CdS, AlN and GaN, plotted against the experimental piezoelectric coefficient (Ref. [34] for AlN and GaN, Ref. [35] for CdS.)

S7 Phonon screening from acoustic modes

As seen in the main manuscript, and specifically, in Figures 3 and 5, acoustic phonons can result in a substantial reduction of the exciton binding energy in CdS and GaN. Moreover, among the systems studied in this work, AlN is the only other case where acoustic phonons contribute to phonon screening. What these materials have in common is that all three are piezoelectric [34, 35], enabling a large coupling of the electrons with acoustic phonons [22], with the average electron-phonon coupling of acoustic modes scaling monotonically with the experimental piezoelectric constants, as seen in Fig. S4.

As shown previously, ignoring quadrupole terms in the Wannier-Fourier interpolation of the electron-phonon matrix elements of acoustic phonons can lead to an overestimation of the magnitude of g in the vicinity of Γ [36]. Therefore, it is possible that inclusion of quadrupole corrections will lead to a modest reduction of the predicted screening of the exciton binding energy by acoustic phonons. Nevertheless, the contribution of acoustic phonons to screening excitons will be important in piezoelectric materials, highlighting the importance of going beyond the simple picture within which optical phonons are the only ones contributing to this effect.

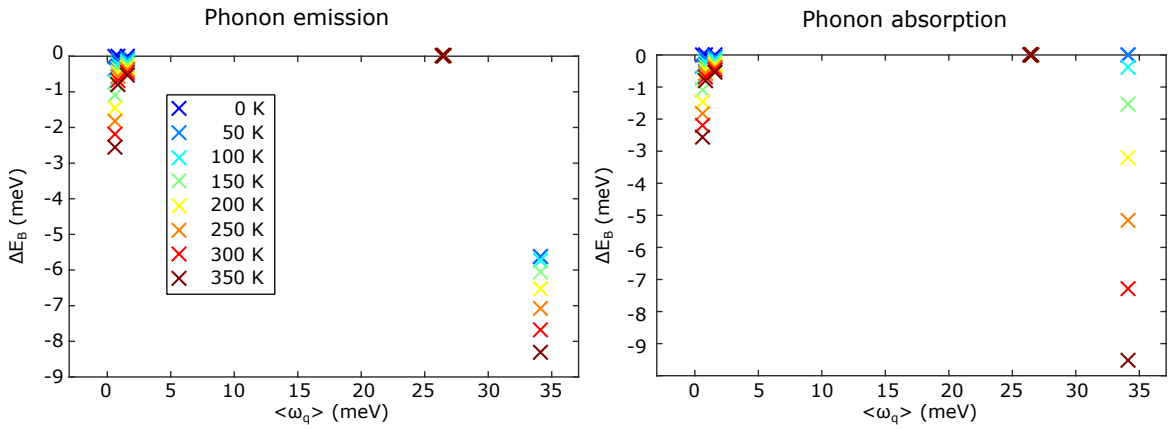

Figure S5 Contribution of emission and absorption of different phonon modes to the exciton binding energy shift of CdS due to phonon screening, as a function of temperature. Here $\langle\omega_q\rangle$ denotes the average frequency of a particular phonon branch.

S8 Phonon screening due to phonon emission and absorption, and wavevector dependence

Eq. (9) of the main manuscript for the phonon kernel allows us to identify the separate contributions of phonon absorption and emission to the phonon kernel. For CdS, we visualize in Fig. S5 the impact of these effects on the exciton binding energy. Notably, phonon emission is already active at low temperatures, while phonon absorption only provides a minor contribution. This is intuitive, as the relevant phonons are unavailable to be absorbed from the environment at low temperatures, according to Eq. (9). The precise temperature where phonons become available to be absorbed may also depend on the level of theory used to obtain phonon frequencies (for example on the exchange-correlation functional [37] or the inclusion of anharmonic effects [38]). Despite this expected sensitivity, we expect the contribution of the absorption term to ΔE_B at small temperatures will be small. On the other hand, the phonon emission term survives even when $N_B(\omega_{\mathbf{q},\nu}, T) \to 0$, and indeed the 0 K results of Table I of the main manuscript are entirely due to phonon emission. As the temperature increases, the contribution of phonon absorption to the screening of the exciton becomes more substantial, and eventually emission and absorption contribute equally.

We also examine the wavevector dependence of the phonon screening correction to the exciton binding energy, for the different phonons of CdS, and at different temperatures, in Figures S6-S9. We see that at low temperatures the emission of high-frequency LO phonons dominates the correction, in agreement with Fig. S5. These polar modes exhibit a Fröhlich-like $1/q$ dependence in their electron-phonon matrix elements, leading the correction to the exciton binding energy to exhibit an overall $1/q^2$ dependence. At higher temperatures low-frequency acoustic phonons start contributing, which generally show a slower decay.

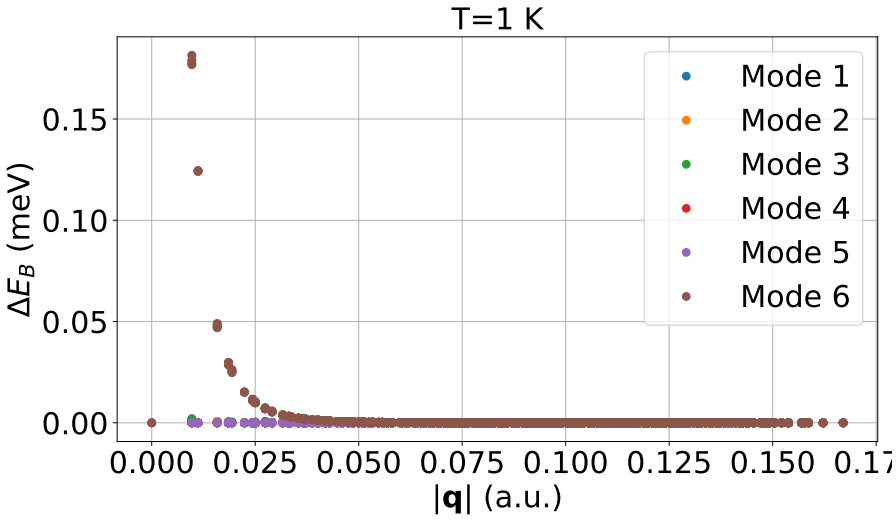

Figure S6 Dependence of the phonon-resolved correction ΔE_B to the exciton binding energy of CdS, as a function of the phonon wavevector $|\mathbf{q}|$, at $T = 1\,\mathrm{K}$.

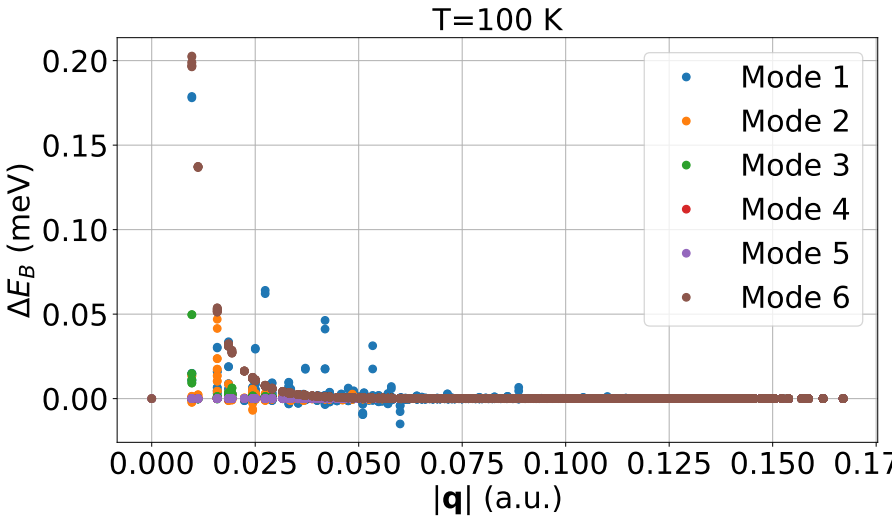

Figure S7 Dependence of the phonon-resolved correction ΔE_B to the exciton binding energy of CdS, as a function of the phonon wavevector $|\mathbf{q}|$, at $T = 100\,\mathrm{K}$.

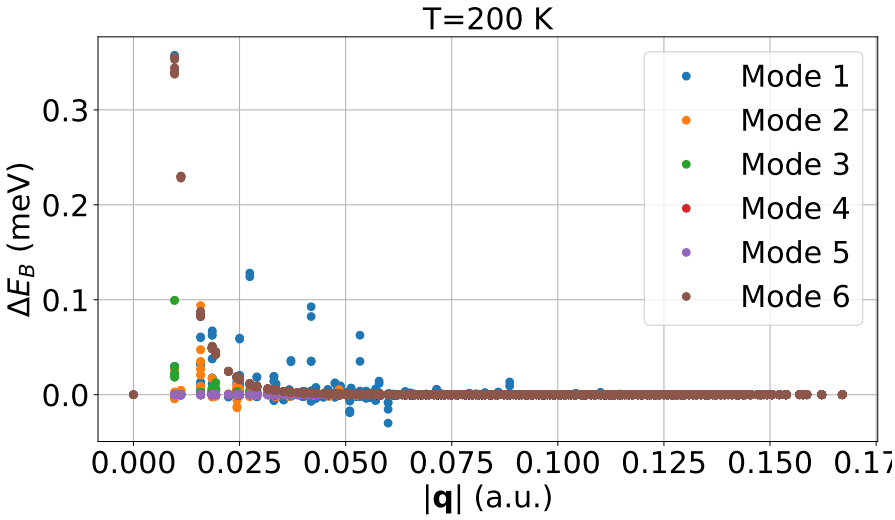

Figure S8 Dependence of the phonon-resolved correction ΔE_B to the exciton binding energy of CdS, as a function of the phonon wavevector $|\mathbf{q}|$, at $T = 200\,\mathrm{K}$.

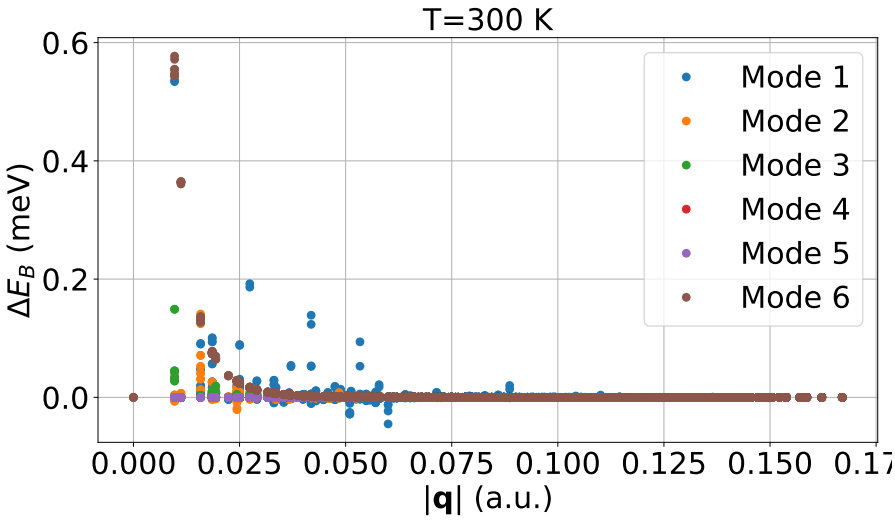

Figure S9 Dependence of the phonon-resolved correction ΔE_B to the exciton binding energy of CdS, as a function of the phonon wavevector $|\mathbf{q}|$, at $T = 300\,\mathrm{K}$.

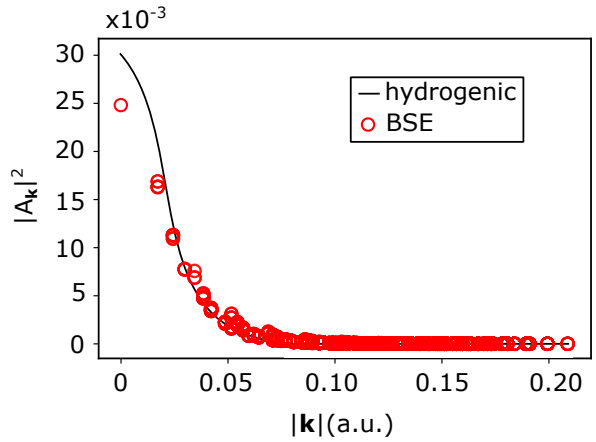

Figure S10 Comparison of the exciton wavefunction in reciprocal space computed within *ab initio* *GW*-BSE and the hydrogenic model for $SrTiO_3$.

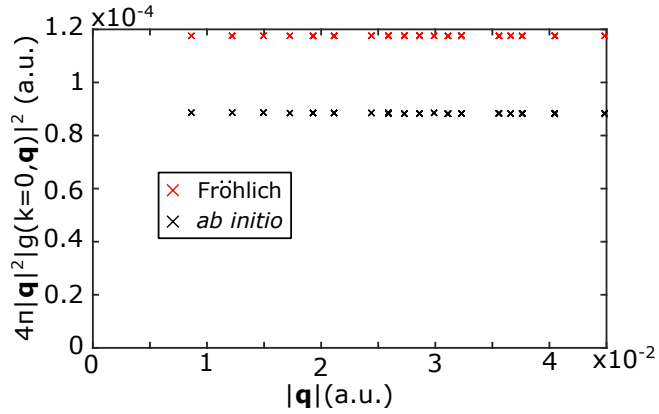

Figure S11 Comparison of the *ab initio* and Fröhlich electron-phonon coupling g of $SrTiO_3$.

S9 Comparison of Fröhlich-hydrogenic approximations to ΔE_B to *ab initio* values in $SrTiO_3$

The model of Eq. (19) of the main manuscript only includes the effect of the highest frequency LO phonon, of 98 meV. One could therefore expect that comparing the value of ΔE_B obtained through the numerical integration of Eq. (19) (-51 meV) to the *ab initio* value which is just due to the highest frequency LO phonon (-36 meV at 0 K) might improve agreement, but in fact it only makes the agreement between the two worse. The derivation of Eq. (19) from the full expression of Eq. (9), relies on two approximations. Specifically, excitons are assumed to be hydrogenic as described within the Wannier-Mott picture, and the electron-phonon interaction is considered

$\omega_{m,\mathbf{q}=\mathbf{0}}$ (meV)	$\Delta\epsilon_m$
20	391.08
57	9.68
98	2.18

Table S4 Phonons with finite contributions to the static dielectric constant ϵ_0 of $SrTiO_3$.

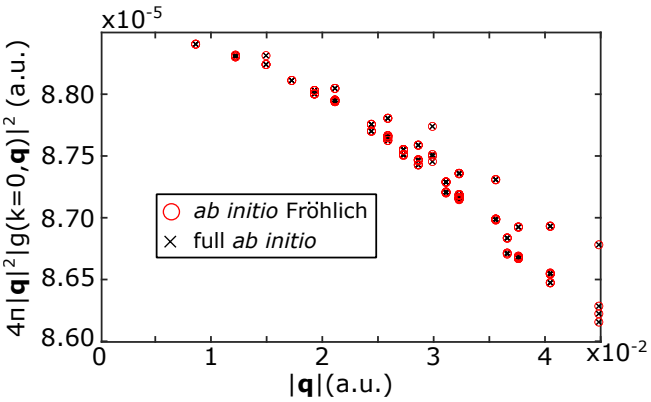

Figure S12 Comparison of the *ab initio* long-range Fröhlich coupling g of Ref. [39] and the full *ab initio* electron-phonon coupling of $SrTiO_3$ for the LO-1 phonon.

to be entirely dominated by the long-range Fröhlich coupling of electrons to LO phonons. Therefore, at least one of these two approximation has to be violated for this system in order to explain the discrepancy between the Fröhlich-hydrogenic $\Delta E_B^{\text{F-H}}$ and first-principles $\Delta E_B^{ab\ initio}$ values of Table I of the main manuscript.

We first examine the validity of the hydrogenic model in $SrTiO_3$. In Fig. S10 we compare the exciton wavefunction as computed within the BSE to the hydrogenic model described by Eq. (18) of the main manuscript, on a Γ-centered patch with a cutoff of 0.15 (in crystal coordinates), which is necessary to satisfy the normalization of the wavefunction within 1%. We see that the two are in good agreement, with some small deviations close to the zone center.

We now move to examine the agreement between the first-principles electron-phonon matrix elements g, and those predicted by the Fröhlich model g_{Fr}, for the LO-1 phonon, in Fig. S11, for a small region close to Γ. It is immediately apparent that the Fröhlich model consistently overestimates the first-principles values for the electron-phonon matrix elements, with the ratio $\frac{g_{Fr}^2}{g^2}$ equal to approximately 4/3. Since the correction to the exciton binding energy is proportional to $|g_{\mathbf{q}\nu}|^2$ it is reasonable to expect a similar overestimation, compared to the *ab initio* value. Indeed, if we naively multiply the first-principles value of −36 meV for the LO-1 phonon by 4/3 we get $\Delta E_B = -48$ meV, in very close agreement to the value of −51 meV predicted by the numerical integration of Eq. (19). Therefore most of the discrepancy can be attributed to the deviations of the Fröhlich vertex from its *ab initio* value, with the remaining difference likely due to the small differences between the hydrogenic and BSE exciton wavefunctions, see Fig. S10.

We now examine the reason behind this observed failure of the Fröhlich model. Unlike other systems studied here and presented in Table I, $SrTiO_3$ is the only material with more than a single LO phonon contributing to phonon screening, as seen in Fig. 9 of the main manuscript, as well as the only system among the studied ones where more than a single phonon mode m contributes to the low-frequency dielectric constant ϵ_0. Following Ref. [40] we decompose ϵ_0 as $\epsilon_0 = \epsilon_\infty + \sum_m \Delta\epsilon_m$, and the phonon modes m with finite $\Delta\epsilon_m$ contribution are given in Table S4, as computed from DFPT. The largest contribution to ϵ_0 comes from the soft polar mode with a frequency of 20 meV at Γ. This phonon does not contribute to the phonon screening of the exciton binding energy, due to its weak electron-phonon coupling around Γ [41], where the exciton coefficients are finite, and

also because of its significantly lower energy compared to the exciton binding energy of 122 meV.

This large contribution to ϵ_0 by a phonon that ultimately does not contribute to phonon screening suggests that using ϵ_0 to estimate the Fröhlich coupling of the LO-1 and LO-2 modes will lead to an overestimation of the vertex g compared to a full first-principles calculation, as indeed we found in Fig. S11. The standard Fröhlich vertex was generalized in Ref. [39] to describe long-range electron-phonon interactions in anisotropic materials and within a mode-resolved picture for each phonon, as given in Eq. (26). This so-called *ab initio* Fröhlich vertex, perfectly reproduces the full first-principles values of the electron- phonon matrix elements close to $\mathbf{q} = \mathbf{0}$, as shown in Fig. S12 for the LO-1 phonon, and the same being true for the LO-2 phonon. This suggests that using Eq. (26) to describe the electron-phonon matrix element in Eq. (19) will restore good agreement between the first-principles $\Delta E_B^{ab\ initio}$ and numerically-integrated value of $\Delta E_{B,\text{gen.}}^{\text{F-H}}$, with the latter now based on the hydrogenic model for excitons and the *generalized* Fröhlich model. Indeed in Table II of the main manuscript we show that by applying these two levels of theory to the phonon modes LO-1 and LO-2, we recover close-to- perfect agreement between the results of Eq. (19) and taking the real part of Eq. (9). Any remaining discrepancy is attributed to the differences between the hydrogenic model and BSE in terms of describing the exciton wavefunction, see Fig. S10.

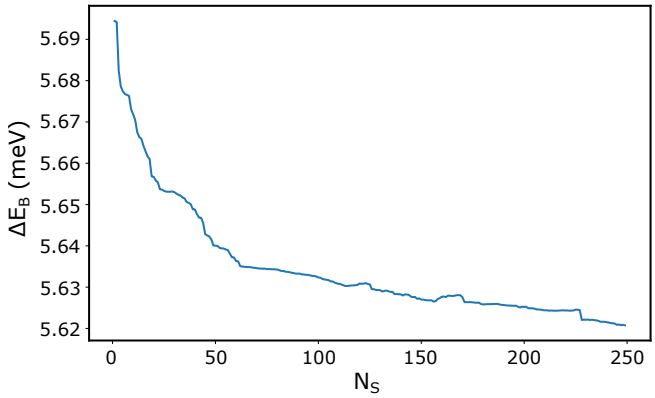

Figure S13 Correction ΔE_B to the exciton binding energy of the first CdS exciton, as a function of the number of excited states N_S.

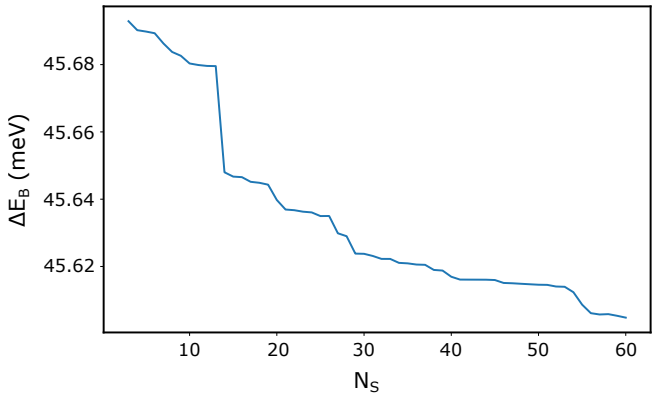

Figure S14 Correction ΔE_B to the exciton binding energy of the first MgO exciton, as a function of the number of excited states N_S.

S10 Convergence of phonon screening with number of excited states

We have examined the effects of the off-diagonal elements of the K^{ph} matrix to all orders, by explicitly diagonalizing the $\Omega_S \delta_{SS'} + K^{ph}_{SS'}(\Omega_S)$ matrix, for an increasing number of excited states N_S. The perturbed eigenvalues are obtained as $\tilde{\Omega}_S$, and the correction due to phonon screening is computed as $\Delta E_B = \tilde{\Omega}_S - \Omega_S$, where Ω_S the bare BSE eigenvalues. We perform this analysis for two systems, CdS and MgO. The correction rapidly converges with the number of excited states included, and even when for CdS we account for the effects of 250 exciton states, the change to ΔE_B compared to only diagonalizing a 3×3 matrix (*i.e.* only including the first three exciton states), and to the first-order perturbative correction reported in our manuscript, is less than 0.1 meV, see Fig. S13. For MgO we included up to 60 states in the perturbation of the bare BSE, and we find the impact of states $4-60$ to be less than 0.1 meV, see Fig. S14. It is therefore safe to include only the first manifold of degenerate excitons in the calculation of K^{ph} and work within first-order perturbation theory for systems with small off-digonal matrix elements, as the ones we study here. It is worth noting that including the effect of off-diagonal terms and higher-lying states results in a very small *reduction* of the phonon-induced correction. This is due to this being a second-order effect, and the perturbation being proportional to $\frac{|K^{ph}_{SS'}(\Omega_S)|^2}{\Omega_S - \Omega'_S}$. For corrections to the lowest-lying excitons, $\Omega_S - \Omega'_S \leq 0$, leading to the small reduction we observe.

References

[1] Anubhav Jain, Shyue Ping Ong, Geoffroy Hautier, Wei Chen, William Davidson Richards, Stephen Dacek, Shreyas Cholia, Dan Gunter, David Skinner, Gerbrand Ceder, and Kristin A. Persson. Commentary: The materials project: A materials genome approach to accelerating materials innovation. *APL Materials*, 1(1), 2013.

[2] Yubo Zhang, Jianwei Sun, John P. Perdew, and Xifan Wu. Comparative first-principles studies of prototypical ferroelectric materials by LDA, GGA, and SCAN meta-GGA. *Physical Review B*, 96(3):1–16, 2017.

[3] P. Giannozzi, S. Baroni, N. Bonini, M. Calandra, R. Car, C. Cavazzoni, D. Ceresoli, G. L. Chiarotti, M. Cococcioni, I. Dabo, A. Dal Corso, S. Fabris, G. Fratesi, S. de Gironcoli, R. Gebauer, U. Gerstmann, C. Gougoussis, A. Kokalj, M. Lazzeri, L. Martin-Samos, N. Marzari, F. Mauri, R. Mazzarello, S. Paolini, A. Pasquarello, L. Paulatto, C. Sbraccia, S. Scandolo, G. Sclauzero, A. P. Seitsonen, A. Smogunov, P. Umari, and R. M. Wentzcovitch. QUANTUM ESPRESSO: a modular and open-source software project for quantum simulations of materials. *Journal of Physics: Condensed Matter*, 21:395502, 2009.

[4] J. P. Perdew, K. Burke, and M. Ernzerhof. Generalized Gradient Approximation Made Simple. *Physical Review Letters*, 77:3865, 1996.

[5] R. O. Jones and O. Gunnarsson. The density functional formalism, its applications and prospects. *Reviews of Modern Physics*, 61(3):689–746, 1989.

[6] D. R. Hamann. Optimized norm-conserving Vanderbilt pseudopotentials. *Physical Review B - Condensed Matter and Materials Physics*, 88(8):1–10, 2013.

[7] M. J. van Setten, M. Giantomassi, E. Bousquet, M. J. Verstraete, D. R. Hamann, X. Gonze, and G. M. Rignanese. The PSEUDODOJO: Training and grading a 85 element optimized norm-conserving pseudopotential table. *Computer Physics Communications*, 226:39–54, 2018.

[8] Jack Deslippe, Georgy Samsonidze, David A. Strubbe, Manish Jain, Marvin L. Cohen, and Steven G. Louie. BerkeleyGW: A massively parallel computer package for the calculation of the quasiparticle and optical properties of materials and nanostructures. *Computer Physics Communications*, 183(6):1269–1289, 2012.

[9] Marina R. Filip, Jonah B. Haber, and Jeffrey B. Neaton. Phonon Screening of Excitons in Semiconductors: Halide Perovskites and beyond. *Physical Review Letters*, 127(6):67401, 2021.

[10] Sebastian E. Reyes-Lillo, Tonatiuh Rangel, Fabien Bruneval, and Jeffrey B. Neaton. Effects of quantum confinement on excited state properties of SrTiO3 from ab initio many-body perturbation theory. *Physical Review B*, 94(4):1–6, 2016.

[11] Mark S. Hybertsen and Steven G. Louie. Electron correlation in semiconductors and insulators: Band gaps and quasiparticle energies. *Physical Review B*, 34(8):5390–5413, 1986.

[12] Antonios M Alvertis, Mauro Del Ben, H Felipe, Diana Y Qiu, Marina R Filip, and Jeffrey B Neaton. Importance of nonuniform Brillouin zone sampling for ab initio Bethe-Salpeter equation calculations of exciton binding energies in crystalline solids. *Physical Review B*, 108(23):1–15, 2023.

[13] Feliciano Giustino, Marvin L. Cohen, and Steven G. Louie. Electron-phonon interaction using Wannier functions. *Physical Review B - Condensed Matter and Materials Physics*, 76(16):1–19, 2007.

[14] Giovanni Pizzi, Valerio Vitale, Ryotaro Arita, Stefan Blügel, Frank Freimuth, Guillaume Géranton, Marco Gibertini, Dominik Gresch, Charles Johnson, Takashi Koretsune, Julen Ibanez-Azpiroz, Hyungjun Lee, Jae Mo Lihm, Daniel Marchand, Antimo Marrazzo, Yuriy Mokrousov, Jamal I. Mustafa, Yoshiro Nohara, Yusuke Nomura, Lorenzo Paulatto, Samuel Poncé, Thomas Ponweiser, Junfeng Qiao, Florian Thöle, Stepan S. Tsirkin, Małgorzata Wierzbowska, Nicola Marzari, David Vanderbilt, Ivo Souza, Arash A. Mostofi, and Jonathan R. Yates. Wannier90 as a community code: New features and applications. *Journal of Physics Condensed Matter*, 32(16), 2020.

[15] S. Ponce, E. R. Margine, C. Verdi, and F. Giustino. EPW: Electron–phonon coupling, transport and superconducting properties using maximally localized Wannier functions. *Computer Physics Communications*, 209:116–133, 2016.

[16] Z. Li, A. M. Alvertis, S. E. Gant, J. B. Neaton, and S. G. Louie. *In preparation.*

[17] Sahar Sharifzadeh, Pierre Darancet, Leeor Kronik, and Jeffrey B. Neaton. Low-Energy Charge-Transfer Excitons in Organic Solids from First-Principles: The Case of Pentacene. *The Journal of Physical Chemistry Letters*, 4:2197–2201, 2013.

[18] S. D. Mahanti and C. M. Varma. Effective Electron-Hole Interactions in Polar Semiconductors. *Physical Review B*, 6(6):2209, 1972.

[19] Jon Lafuente-Bartolome, Chao Lian, Weng Hong Sio, Idoia G. Gurtubay, Asier Eiguren, and Feliciano Giustino. Unified approach to polarons and phonon-induced band structure renormalization. *Physical Review Letters*, 129(7):76402, 2022.

[20] S. D. Mahanti and C. M. Varma. Effective electron an hole interactions in a polarizable field. *Physical Review Letters*, 25(16):1115, 1970.

[21] J. Pollmann and H. Büttner. Effective Hamiltonians and bindings energies of Wannier excitons in polar semiconductors. *Physical Review B*, 16(10):4480–4490, 1977.

[22] Gerald D Mahan. *Many-Particle Physics*. Physics of Solids and Liquids. Springer, 2013.

[23] Michael E. Peskin and Daniel V. Schroeder. *An Introduction to Quantum Field Theory*. Taylor & Francis group, 1995.

[24] Raül Perea-Causín, Samuel Brem, and Ermin Malic. Phonon-assisted exciton dissociation in transition metal dichalcogenides. *Nanoscale*, 13(3):1884–1892, 2021.

[25] B. A. Lippmann. Rearrangement Collisions. *Physical Review*, 102:264, 1956.

[26] Sigenobu Sunakawa. On the Theory of Rearrangement Collisions. *Progress of Theoretical Physics*, 24(5):963, 1960.

[27] T. B. Day, L.S. Rodberg, G.A. Snow, and J. Sucher. Note on Rearrangement Collisions. *Physical Review*, 123(3):1051–1053, 1961.

[28] C. Coveney, J.B. Haber, A. M. Alvertis, J. B. Neaton, and M. R. Filip. *In preparation*.

[29] H. Kröncke, S. Figge, B. M. Epelbaum, and D. Hommel. Determination of the temperature dependent thermal expansion coefficients of bulk AlN by HRXRD. *Acta Physica Polonica A*, 114(5):1193–1200, 2008.

[30] D Strauch. *CdS: thermal expansion*, pages 97–98. Springer Berlin Heidelberg, Berlin, Heidelberg, 2012.

[31] C. Roder, S. Einfeldt, S. Figge, and D. Hommel. Temperature dependence of the thermal expansion of GaN. *Physical Review B - Condensed Matter and Materials Physics*, 72(8):1–6, 2005.

[32] Nicholas C. Corsepius, Thomas C. DeVore, Barbara A. Reisner, and Deborah L. Warnaar. Using variable temperature powder X-ray diffraction to determine the thermal expansion coefficient of solid MgO. *Journal of Chemical Education*, 84(5):818–821, 2007.

[33] A. Boudali, M. Driss Khodja, B. Amrani, D. Bourbie, K. Amara, and A. Abada. First-principles study of structural, elastic, electronic, and thermal properties of SrTiO3 perovskite cubic. *Physics Letters, Section A: General, Atomic and Solid State Physics*, 373(8-9):879–884, 2009.

[34] C. M. Lueng, H. L.W. Chan, W. K. Fong, C. Surya, and C. L. Choy. Piezoelectric coefficients of aluminum nitride and gallium nitride. *Journal of Applied Physics*, 88(9):5360, 2000.

[35] Xuewen Wang, Xuexia He, Hongfei Zhu, Linfeng Sun, Wei Fu, Xingli Wang, Lai Chee Hoong, Hong Wang, Qingsheng Zeng, Wu Zhao, Jun Wei, Zhong Jin, Zexiang Shen, Jie Liu, Ting Zhang, and Zheng Liu. Subatomic deformation driven by vertical piezoelectricity from CdS ultrathin films. *Science Advances*, 2(7):1–10, 2016.

[36] Vatsal A. Jhalani, Jin Jian Zhou, Jinsoo Park, Cyrus E. Dreyer, and Marco Bernardi. Piezoelectric Electron-Phonon Interaction from Ab Initio Dynamical Quadrupoles: Impact on Charge Transport in Wurtzite GaN. *Physical Review Letters*, 125(13):136602, 2020.

[37] Kerstin Hummer, Judith Harl, and Georg Kresse. Heyd-Scuseria-Ernzerhof hybrid functional for calculating the lattice dynamics of semiconductors. *Physical Review B - Condensed Matter and Materials Physics*, 80(11), 2009.

[38] Michele Lazzeri, Matteo Calandra, and Francesco Mauri. Anharmonic phonon frequency shift in MgB2. *Physical Review B - Condensed Matter and Materials Physics*, 68(22):2–5, 2003.

[39] Carla Verdi and Feliciano Giustino. Fröhlich electron-phonon vertex from first principles. *Physical Review Letters*, 115(17):1–5, 2015.

[40] Craig Fennie and Karin Rabe. Structural and dielectric properties of Sr2TiO4 from first principles. *Physical Review B - Condensed Matter and Materials Physics*, 68(18):1–9, 2003.

[41] Jin Jian Zhou, Olle Hellman, and Marco Bernardi. Electron-Phonon Scattering in the Presence of Soft Modes and Electron Mobility in SrTiO3 Perovskite from First Principles. *Physical Review Letters*, 121(22):226603, 2018.